Inorganic Chemistry

Article

pubs.acs.org/IC

X-ray Crystallographic, Multifrequency Electron Paramagnetic Resonance, and Density Functional Theory Characterization of the $Ni(P^{Cy}_2N^{tBu}_2)_2^{n+}$ Hydrogen Oxidation Catalyst in the Ni(I) Oxidation State

Jens Niklas,[†] Mark Westwood,[‡] Kristy L. Mardis,[§] Tiara L. Brown,[§] Anthony M. Pitts-McCoy,[§] Michael D. Hopkins,*[,‡] and Oleg G. Poluektov*[,†]

[†]Division of Chemical Sciences and Engineering, Argonne National Laboratory, Argonne, Illinois 60439, United States

[‡]Department of Chemistry, The University of Chicago, Chicago, Illinois 60637, United States

[§]Department of Chemistry and Physics, Chicago State University, Chicago, Illinois 60628, United States

Supporting Information

ABSTRACT: The Ni(I) hydrogen oxidation catalyst $[Ni(P^{Cy}_2N^{tBu}_2)_2]^+$ ($\mathbf{1}^+$; $P^{Cy}_2N^{tBu}_2$ = 1,5-di(*tert*-butyl)-3,7-dicyclohexyl-1,5-diaza-3,7-diphosphacyclooctane) has been studied using a combination of electron paramagnetic resonance (EPR) techniques (X-, Q-, and D-band, electron−nuclear double resonance, hyperfine sublevel correlation spectroscopy), X-ray crystallography, and density functional theory (DFT) calculations. Crystallographic and DFT studies indicate that the molecular structure of $\mathbf{1}^+$ is highly symmetrical. EPR spectroscopy has allowed determination of the electronic **g** tensor and the spin density distribution on the ligands, and revealed that the Ni(I) center does not interact strongly with the potentially coordinating solvents acetonitrile and butyronitrile. The EPR spectra and magnetic parameters of $\mathbf{1}^+$ are found to be distinctly different from those for the related compound $[Ni(P^{Ph}_2N^{Ph}_2)_2]^+$ ($\mathbf{4}^+$). One significant contributor to these differences is that the molecular structure of $\mathbf{4}^+$ is unsymmetrical, unlike that of $\mathbf{1}^+$. DFT calculations on derivatives in which the R and R′ groups are systematically varied have allowed elucidation of structure/substituent relationships and their corresponding influence on the magnetic resonance parameters.

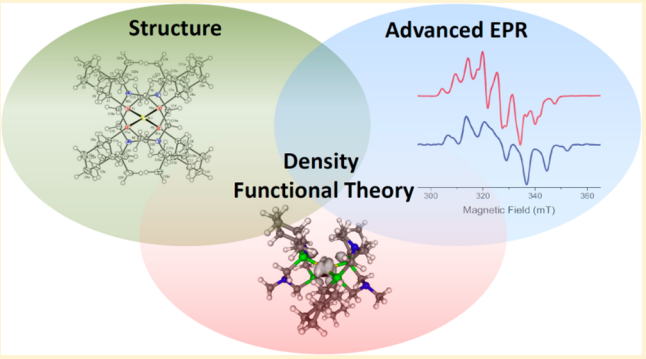

INTRODUCTION

The environmental and social impacts of fossil fuel consumption require that we develop renewable sources of energy.[1−3] The prospect of using molecular hydrogen as a renewable fuel has motivated considerable research into the development of efficient homogeneous catalysts for the reduction of protons to H_2 and for the corresponding reverse H_2 oxidation reaction.[4−10] In general, catalysts that employ first-row transition metals are especially attractive targets owing to their greater natural abundance and potential lower cost relative to those of traditional catalysts comprised of rare and expensive metals such as platinum. Relevant to this goal, DuBois, Bullock, and co-workers have pioneered the development of highly active and tunable nickel−phosphine electrocatalysts of the general form $[Ni(P^R_2N^{R'}_2)_2]^{n+}$ (n = 0, 1, 2).[11−14] These catalysts, examples of which are shown schematically in Chart 1 (for n = 1), contain second-coordination-sphere amine groups that are integral to the H−H bond-forming and -cleavage processes.[13,15,16] The nature of the R and R′ substituents on the phosphine and amine units, respectively, governs whether these catalysts operate for proton reduction, hydrogen oxidation, or the bidirectional redox interconversion of protons and hydrogen.[11,17] Extensive studies

Chart 1. $[Ni(P^R_2N^{R'}_2)_2]^+$ Complexes Discussed in This Paper

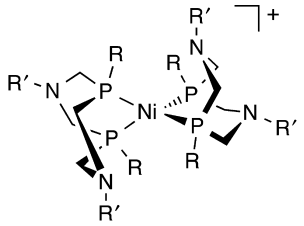

Compound	R	R′
$\mathbf{1}^+$	Cy	*t*-Bu
$\mathbf{2}^+$	Ph	*t*-Bu
$\mathbf{3}^+$	Cy	Ph
$\mathbf{4}^+$	Ph	Ph
$\mathbf{5}^+$	Ph	$C_6H_4CH_2P(O)(OEt)_2$

Received: February 25, 2015
Published: June 22, 2015

DOI: 10.1021/acs.inorgchem.5b00445
Inorg. Chem. 2015, 54, 6226−6234

of these catalysts have provided detailed insights into how the phosphine and amine substituents affect the redox potentials, Brønsted acidity, substrate binding free energies, and other underlying thermodynamic factors that control catalyst function. These details are particularly rich for catalyst intermediates in the Ni(II) and Ni(0) oxidation states, which are amenable to study by multinuclear NMR spectroscopic methods.[18]

It has been found that complexes of the form $[Ni(P^R_2N^{R'}_2)_2]^+$, which possess the Ni(I) oxidation state, are key intermediates in the catalytic cycles for both proton reduction and hydrogen oxidation by this class of catalysts.[15,18,19] In the catalytic oxidation of hydrogen, the one-electron oxidation of $[Ni(P^R_2N^{R'}_2)_2]^+$ compounds produces the $[Ni(P^R_2N^{R'}_2)_2]^{2+}$ species that coordinate dihydrogen, while, in catalytic proton reduction, $[Ni(P^R_2N^{R'}_2)_2]^+$ species initiate the cycle by binding the first proton. The molecular and electronic structures of paramagnetic Ni(I) species have not been investigated as extensively as those of diamagnetic intermediates; e.g., they are not fruitfully probed by NMR spectroscopic techniques due to their paramagnetism (d^9 electron configuration). In contrast, electron paramagnetic resonance (EPR) spectroscopy is an excellent tool for characterizing the electronic structures of paramagnetic metal complexes and studying changes due to the variation of ligands and the surroundings.[20−23] Recently, two EPR studies on $[Ni(P^R_2N^{R'}_2)_2]^+$ proton reduction catalysts $\mathbf{4}^+$ [24] and $\mathbf{5}^+$ [25] (Chart 1) have been reported. Among several observations, it was found that the phosphorus nuclei of these complexes are structurally and magnetically inequivalent. Furthermore, it was noted that there is appreciable delocalization of the unpaired electron spin density onto the ligands. These and related[26] studies show that EPR spectroscopy is a sensitive and useful probe for Ni(I) species in the $[Ni(P^R_2N^{R'}_2)_2]^{n+}$ family of catalysts.

There have not yet been corresponding EPR spectroscopic studies of $[Ni(P^R_2N^{R'}_2)_2]^+$ complexes that function as hydrogen oxidation catalysts. These catalysts, of which the complex $[Ni(P^{Cy}_2N^{tBu}_2)_2][BF_4]$ ($\mathbf{1}[BF_4]$; $P^{Cy}_2N^{tBu}_2$ = 1,5-di(*tert*-butyl)-3,7-dicyclohexyl-1,5-diaza-3,7-diphosphacyclooctane) has been found to exhibit particularly high activity,[18,27] generally possess more strongly electron-donating phosphine R groups than do proton reduction catalysts (e.g., R = Cy for $\mathbf{1}^+$ vs R = Ph for $\mathbf{4}^+$ and $\mathbf{5}^+$). In addition to governing catalytic activity through control of the thermodynamic factors noted above, these different substituents also likely affect the molecular structures of the catalyst, the interaction of the Ni center with the solvent (which can influence catalytic activity),[28] and the delocalization of the unpaired electron. The contributions to these effects from catalytic intermediates in the Ni(I) state have not been directly probed.

Here we report a study of $\mathbf{1}[BF_4]$ using X-ray crystallography, density functional theory (DFT) calculations, and EPR spectroscopic methods. We use EPR spectroscopy at X-band (9−10 GHz), Q-band (34 GHz), and D-band (130 GHz) microwave frequencies to distinguish clearly between field-dependent and field-independent parameters. The multifrequency approach allows us to determine **g** tensor anisotropy and hyperfine splitting due to the ^{31}P, ^{14}N, and ^1H magnetic nuclei of the ligands. The crystallographic, computational, and EPR spectroscopic studies all indicate that the structure of the $\mathbf{1}^+$ ion is highly symmetric. This contrasts with the structure of $\mathbf{4}^+$, which is inferred to be less symmetrical and to possess several energetically accessible conformers. It is additionally found that the Ni(I) center of $\mathbf{1}^+$ interacts only weakly with solvent, and that the magnitude of the hyperfine coupling of the Ni(I) electron spin with the phosphorus nuclei differs significantly from those observed previously for $\mathbf{4}^+$. Computational studies of $[Ni(P^R_2N^{R'}_2)_2]^+$ compounds in which the phosphine R and amine R′ substituents of $\mathbf{1}^+$ and $\mathbf{4}^+$ are systematically interchanged ($\mathbf{2}^+$ and $\mathbf{3}^+$, Chart 1) allow delineation of their individual and collective effects on the molecular structures and magnetic parameters of the catalysts.

EXPERIMENTAL METHODS

General Procedures for Synthesis and Characterization. All experiments were performed under a nitrogen atmosphere using standard Schlenk and glovebox techniques. Solvents used for syntheses were HPLC grade; they were further purified by passing them under nitrogen pressure through an anaerobic, stainless-steel system consisting of either two 4.5 in. × 24 in. (1 gal) columns of activated A2 alumina (CH_3CN, Et_2O, and CH_2Cl_2) or one column of activated A2 alumina and one column of activated BASF R3-11 catalyst (*n*-pentane).[29] Butyronitrile and CD_3CN were stored under nitrogen over activated 4 Å molecular sieves. The compounds $\mathbf{1}$[18] and $\mathbf{1}[BF_4]_2$[27] were prepared by standard procedures. ^1H and $^{31}P\{^1H\}$ NMR spectra were recorded at room temperature with a Bruker DRX 400 NMR spectrometer. Chemical shifts were measured relative to the solvent resonance (^1H)[30] or an external standard of 85% H_3PO_4 (^{31}P). Single-crystal X-ray diffraction studies were performed using a Bruker D8 Venture system; full details are available in the Supporting Information.

Preparation of $\mathbf{1}[BF_4]$. This compound was prepared by a modified version of the previously reported procedure.[18] A mixture of $\mathbf{1}$ (0.100 g, 0.11 mmol) and $\mathbf{1}[BF_4]_2$ (0.107 g, 0.099 mmol) in CH_3CN (10 mL) was stirred at room temperature for 30 min. The $^{31}P\{^1H\}$ NMR spectrum of the reaction mixture showed that $\mathbf{1}[BF_4]_2$ had been completely consumed and exhibited a weak signal due to the small excess quantity of $\mathbf{1}$ employed in the starting mixture. The solvent was removed under reduced pressure, and the remaining orange residue was stirred for 1 h while suspended in *n*-pentane (30 mL) to extract unreacted $\mathbf{1}$. An orange powder was collected by filtration, washed with pentane (3 × 10 mL), and dried under vacuum. The product was recrystallized by vapor diffusion of Et_2O into a concentrated solution of the compound in CH_3CN (ca. 3 mL); this provided, after 3 days, green crystals of $\mathbf{1}[BF_4]$ (0.130 g, 63% yield) suitable for single-crystal X-ray diffraction experiments. ^1H NMR (400.1 Hz, CD_3CN): δ 3.99 (v br), 1.70 (br), 1.42 (br), 0.96 (br).

Multifrequency EPR Studies. All samples were prepared under a nitrogen atmosphere. Solutions of $\mathbf{1}[BF_4]$ (∼2 mM) were contained in Suprasil quartz capillaries; X-band sample tubes had a 4 mm outside diameter (o.d.), Q-band sample tubes a 2 mm o.d., and D-band sample tubes a 0.6 mm o.d. The filled EPR sample tubes were sealed under nitrogen to prevent exposure to air. However, in the case of the fine-bore D-band tubes, which are difficult to seal, some exposure to air could not be avoided; this resulted in generation of a trace paramagnetic impurity (see the Results and Discussion).

Continuous wave (CW) X-band (9−10 GHz) EPR experiments were carried out with a Bruker ELEXSYS E580 EPR spectrometer (Bruker Biospin, Rheinstetten, Germany), equipped with a TE_{102} rectangular EPR resonator (Bruker ER 4102st) and a helium gas-flow cryostat (ICEoxford, U.K.). An intelligent temperature controller (ITC503) from Oxford Instruments (Oxford, U.K.) was used.

Pulsed X-band experiments were performed on the same spectrometer, using a Flexline dielectric ring resonator (Bruker ER 4118X-MD5-W1 or EN 4118X-MD4-W1) and a helium gas-flow cryostat (CF935, Oxford Instruments). The temperature was controlled by an ITC503 (Oxford Instruments). Pulsed electron−nuclear double resonance (ENDOR) experiments were performed on the same spectrometer using a Bruker EN 4118X-MD4-W1 resonator

DOI: 10.1021/acs.inorgchem.5b00445
Inorg. Chem. 2015, 54, 6226−6234

and a BT01000-AlphaSA 1 kW radio frequency (rf) amplifier (TOMCO Technologies, Stepney, Australia). The Davies ENDOR sequence[31,32] ($\pi-t-\pi/2-\tau-\pi-\tau-$echo) with an inversion π pulse of 148 ns, t = 10 μs, and the Mims ENDOR sequence[32,33] ($\pi/2-\tau-\pi/2-t-\pi/2-\tau-$echo) with a $\pi/2$ pulse of 24 ns, t = 10 μs, were employed. The rf pulse was 6 μs long.

Continuous wave (CW) Q-band (34 GHz) EPR experiments were carried out with the same EPR spectrometer, equipped with a Q-band bridge (Bruker ER 051 QG), a cylindrical EPR resonator (Bruker ER 5106 QT-W), and a helium gas-flow cryostat (CF935, Oxford Instruments). The temperature was controlled by an ITC503 (Oxford Instruments). The microwave (MW) frequency was monitored by a frequency counter (5352B, Hewlett-Packard). The spectra were recorded under saturating conditions, yielding absorption-type line shapes, and were then pseudomodulated[34] to yield derivative-type line shapes.

High-frequency EPR measurements were performed on a home-built D-band (130 GHz) spectrometer equipped with a single-mode TE_{011} cylindrical cavity.[35,36] The spectrometer was controlled by a PC using the SpecMan4EPR program.[37] EPR spectra were recorded in pulsed mode to remove the microwave phase distortion due to fast-passage effects. The absorption line shape of the EPR spectra was recorded by monitoring the electron spin echo (ESE) intensity from a two-microwave-pulse sequence as a function of the magnetic field. The duration of a $\pi/2$ microwave pulse was 40−60 ns, and typical separation times between microwave pulses were 150−300 ns. All D-band spectra have been pseudomodulated to yield derivative-type line shapes.[34]

Data processing was done as described previously[38] using Xepr (Bruker BioSpin) and Matlab 7.11.2 (MathWorks, Natick, MA) software. The magnetic parameters were obtained from theoretical simulation of the EPR and ENDOR spectra. The simulations were performed using the EasySpin software package (version 4.5.5).[39] The accuracy in determination of the electronic **g** tensor for the set of multifrequency EPR spectra is estimated to be ±0.001.

DFT Calculations. The molecular structures of $\mathbf{1}^+$, $\mathbf{2}^+$, $\mathbf{3}^+$, and $\mathbf{4}^+$ were optimized *in vacuo* using PQS v 2.0-3.[40] Basis sets and functionals used for geometry optimizations were selected on the basis of a benchmarking study described below. In all cases frequency calculations were performed to ensure, by the absence of imaginary frequencies, that the stationary points obtained in the geometry optimizations were energetic minima. EPR parameters were calculated using the computational package Orca 2.9.1.[41] The principal g values were calculated employing the coupled perturbed Kohn−Sham equations.[42] The anisotropic magnetic dipole and the isotropic Fermi contact contributions to the hyperfine coupling were calculated for all ^{1}H, ^{14}N, and ^{31}P atoms. Second-order spin−orbit hyperfine contributions were included for ^{31}P atoms. Calculations of the EPR parameters employed the B3LYP functional,[43−46] the EPRII basis set[47,48] for C, N, and H, the IGLOII basis set[49] for P, and the Wachters basis set[50−52] for Ni. To test for the influence of the basis set on the calculated EPR parameters, additional single-point calculations were performed using the def2-TZVP basis set[53] for all atoms; these showed only minor differences in the magnetic parameters (**g** tensors, hyperfine interaction tensors (**A** tensors); see the Supporting Information, Table S3).

To determine the best method for geometry optimization, the structure of $\mathbf{1}^+$ was optimized *in vacuo* using multiple basis sets (3-21G, 6-31G) and functionals (B3LYP, BP86, PBE); in each case, the geometry from the crystal structure of $\mathbf{1}[BF_4]$ served as the starting point. In general, these methods provided Ni−P bond distances slightly longer than those determined from the crystal structure of $\mathbf{1}^+$ (Supporting Information, Table S4), with the 3-21G basis set providing closer agreement than 6-31G for a given functional. Subsequent calculation of the EPR parameters (g values and ^{31}P isotropic hyperfine coupling constants) for each structure showed that the results for the structures provided by the functionals BP86 and PBE are very similar to each other and close to the experimental values. The structures provided by calculations using the B3LYP functional give larger g values and smaller hyperfine constants in the subsequent EPR parameter calculations. As a consequence of these considerations, the BP86 functional and 3-21G basis set were used for geometry optimizations of $\mathbf{1}^+$, $\mathbf{2}^+$, $\mathbf{3}^+$, and $\mathbf{4}^+$ because they provide a good balance of speed and accuracy. The starting structures for $\mathbf{2}^+$, $\mathbf{3}^+$, and $\mathbf{4}^+$ were obtained by substituting R and R′ in the optimized structure of complex $\mathbf{1}^+$. Atomic coordinates of optimized structures and calculated magnetic resonance parameters are given in the Supporting Information (Tables S8−S25).

RESULTS AND DISCUSSION

Molecular Structure of $\mathbf{1}^+$. The molecular structures of $\mathbf{1}^+$ in the solid state and gas phase were determined using X-ray crystallography and DFT calculations, respectively. The X-ray crystal structure of $\mathbf{1}[BF_4]$ shows the presence of discrete $\mathbf{1}^+$ and BF_4^- ions; the former is displayed in Figure 1 (see also the Supporting Information, Figure S1). The Ni(I) center of $\mathbf{1}^+$ exhibits a distorted tetrahedral geometry, with an intraligand P−Ni−P bite angle of 81.8° and with the P−Ni−P planes of the two ligands offset by a dihedral angle (α) of 62.1° (where α = 90° characterizes a NiP_4 subunit with D_{2d} symmetry). The NiP_4 subunit is quite symmetric: the $\mathbf{1}^+$ ion resides at a site of 2-fold rotational symmetry, and the non-symmetry-equivalent Ni−P bonds differ in length by less than 2σ (2.2175(7) and 2.2195(7) Å). The high symmetry about the Ni center of $\mathbf{1}^+$ may be contrasted with findings for the related Ni(I) compound $[Ni(P^{tBu}{}_2N^{Bn}{}_2)_2][BF_4]$,[54] the crystal structure of which exhibits statistically significant differences among the Ni−P bond lengths (2.2113(15), 2.2124(17), 2.2289(15), and 2.2292(16) Å), and for structures calculated for $\mathbf{4}^+$ using DFT (see below). In $\mathbf{1}[BF_4]$ the four six-membered $[NiPCH_2NCH_2P]$ rings formed by the chelating ligands are in the boat conformation. The long Ni···N distances (Ni−N(1) = 3.412 Å, Ni−N(2) = 3.411 Å) indicate that the pendant amine groups are not bonded to the nickel center.

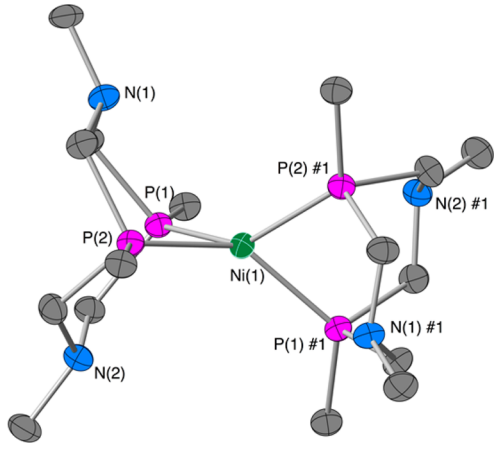

Figure 1. Thermal ellipsoid representation of the core of the $\mathbf{1}^+$ ion of $\mathbf{1}[BF_4]$ (50% probability ellipsoids). Carbon (gray), phosphorus (purple), nitrogen (blue), and nickel (green) atoms are shown; for clarity, hydrogen atoms are omitted and only the first carbon atoms of the cyclohexyl and *tert*-butyl groups are shown. Selected bond lengths (Å) and bond angles (deg): Ni(1)−P(1) = 2.2175(7), Ni(1)−P(2) = 2.2195(7), P(1)−Ni(1)−P(2) = 81.83(3), P(1)−Ni(1)−P(1)#1 = 111.36(4), P(2)−Ni(1)−P(2)#1 = 112.13(3), P(1)−Ni(1)−P(2)#1 = 140.49(2), α = 62.1°. Complete metrical data are provided in the Supporting Information (Table S2 and Figure S1).

The gas-phase molecular structure of $\mathbf{1}^+$ provided by DFT calculations (Supporting Information, Table S8) is in essential

DOI: 10.1021/acs.inorgchem.5b00445
Inorg. Chem. 2015, 54, 6226−6234

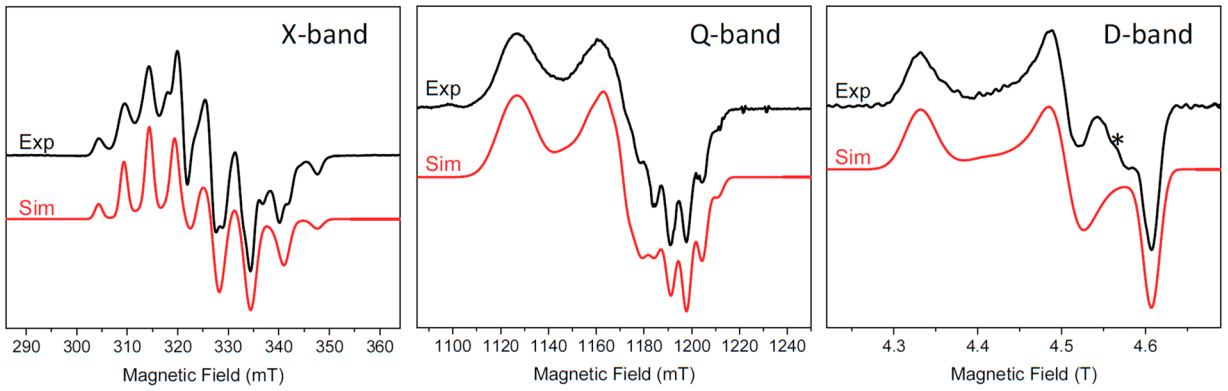

Figure 2. Electron paramagnetic resonance spectra (X-, Q-, and D-band) of a 2 mM solution of **1**[BF_4] in butyronitrile at 10 K (black, experimental spectra; red, simulations). Magnetic resonance parameters used for the simulations are provided in Table 1. The X-band EPR spectrum was recorded in continuous wave (CW) mode; thus, the spectrum represents the first derivative of an absorption spectrum. The Q-band and D-band measurements generated absorption-type spectra, but were pseudomodulated[34] to yield derivative-type spectra. The asterisk marks the EPR signal of an additional paramagnetic species, probably due to decomposition of $\mathbf{1}^+$; see the Experimental Methods.

Table 1. Electron Paramagnetic Resonance Parameters of $[Ni(P^R{}_2N^{R'}{}_2)_2]^+$ Complexes

complex	solvent(s)	g value (±0.001)	^{31}P hyperfine coupling constant (MHz)	ref
1[BF_4]	butyronitrile	2.146, 2.063, 2.017	150, 160, 185[a]	this work
1[BF_4]	MeCN/CH_2Cl_2 (1:2)	2.146, 2.062, 2.017	150, 160, 185[a]	this work
4[BF_4]	toluene/pyridine	2.104, 2.070, 2.006	210, 220, 220[a]	24
5[BF_4]	MeCN (with pyridine)	2.15, 2.07, 2.00[b]	190, 209, 224, 230[c]	25

[a]Principal components of four equivalent ^{31}P hyperfine coupling tensors. [b]**g** tensor not spectroscopically resolved, but obtained by a multiparameter fit of the X-band EPR spectrum, assuming isotropic ^{31}P hyperfine coupling, value ± 0.01. [c]Isotropic hyperfine coupling constants, four nonequivalent ^{31}P nuclei.

agreement with the solid-state structure of **1**[BF_4] described above. The calculated Ni−P bond distance, intraligand P−Ni−P bond angle, and interligand dihedral angle all differ slightly from those observed in the crystal structure (calculated/experimental values: Ni−P = 2.225/2.2185$_{av}$ Å; P−Ni−P = 83.8/81.8°; α = 69.1/62.1°), which in part may reflect the effects of crystal packing. Importantly, though, the calculated structure very nearly conforms to idealized D_2 symmetry, with the phosphorus nuclei residing in chemically equivalent positions. This is consistent with the observation from the crystal structure of a highly symmetric structure, and contrasts with observations for $\mathbf{4}^+$ described below. The six-membered rings formed by the chelating ligands are all computed to adopt a boat conformation, as found in the crystal structure.

The geometry about the Ni(I) center of **1**[BF_4] may be compared with those previously determined by X-ray crystallography for the redox-congeneric Ni(II) and Ni(0) compounds $[Ni(P^{Cy}{}_2N^{tBu}{}_2)_2][BF_4]_2$ (**1**[BF_4]$_2$)[27] and Ni($P^{Cy}{}_2N^{tBu}{}_2$)$_2$ (**1**),[18] respectively. The interligand dihedral angles of these compounds vary with the d^n configuration in the expected manner, with the geometry of d^{10} **1** lying closer to the tetrahedral limit (α = 85°) than that of d^9 $\mathbf{1}^+$ (α = 62.1°), and d^8 $\mathbf{1}^{2+}$ lying closer to the square-planar limit (α = 23°). The Ni−P bonds lengthen with increasing oxidation state (d(Ni−P)$_{av}$: **1**, 2.1394 Å, $\mathbf{1}^+$, 2.2185 Å, $\mathbf{1}^{2+}$, 2.2277 Å), and the intraligand P−Ni−P angle decreases concomitantly (∠P−Ni−P: **1**, 83.9°; $\mathbf{1}^+$, 81.8°; $\mathbf{1}^{2+}$, 80.8°). These trends in bond lengths and bond and dihedral angles were also seen for the Ni(I)/Ni(0) pair of compounds $[Ni(P^{tBu}{}_2N^{Bn}{}_2)_2][BF_4]$ and Ni($P^{tBu}{}_2N^{Bn}{}_2$)$_2$.[54]

Multifrequency EPR Study of 1[BF_4] in Frozen Solution. Figure 2 shows the EPR spectra of frozen solutions of **1**[BF_4] in butyronitrile at X-band (9−10 GHz), Q-band (34 GHz), and D-band (130 GHz) frequencies. All EPR spectra are depicted as derivative-type spectra; i.e., they are the first derivative of an absorption spectrum. Measurements at different cryogenic temperatures (in the 5−100 K range) revealed no temperature dependence of the EPR spectrum (Supporting Information, Figure S2), allowing us to use the optimal temperature for each type of experiment.

The comparison of the X-band spectra recorded in pulsed mode with those recorded in CW mode revealed no significant difference (after integration of the CW spectrum or pseudomodulation of the pulsed spectra; see the Supporting Information, Figure S3). This assures that the pulsed experiments probe the same molecules as the CW experiments; thus, conclusions drawn from analyses of the pulsed experiments can be transferred to the CW experiments. The relatively long relaxation times at low temperatures (T < 20 K) demonstrate that we were observing individual nickel complexes and not multimers/aggregates (Supporting Information, Figure S4).

The X-band EPR spectrum of $\mathbf{1}^+$ exhibits higher resolution than those previously reported for $[Ni(P^R{}_2N^{R'}{}_2)_2]^+$ complexes $\mathbf{4}^+$[24] and $\mathbf{5}^+$,[25] indicating it possesses a well-defined geometry even in frozen solution. The complicated X-band EPR spectrum is caused by the substantial anisotropy of the electronic **g** tensor and the hyperfine interaction with the four ^{31}P nuclei (I = 1/2, 100% natural abundance), which is comparable in magnitude to the **g** tensor anisotropy. The pattern indicates that all four phosphorus nuclei are strongly coupled to the unpaired electron, and that the hyperfine interaction contains both significant isotropic and anisotropic parts. Hyperfine interactions with other magnetic nuclei (^{1}H, ^{14}N, ^{13}C) are not resolved at any of the three microwave

DOI: 10.1021/acs.inorgchem.5b00445
Inorg. Chem. 2015, 54, 6226−6234

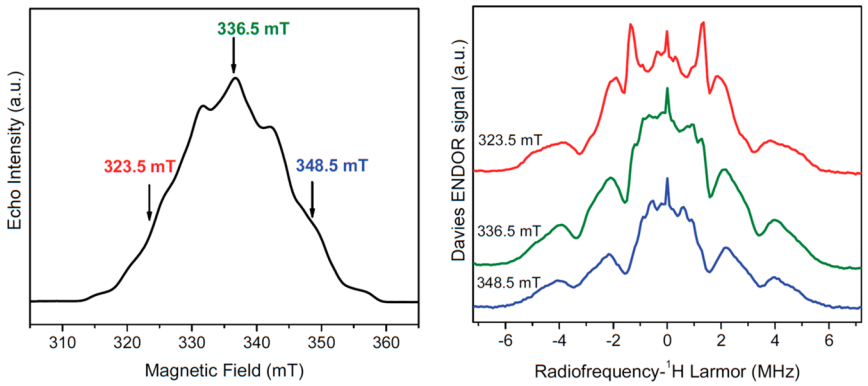

Figure 3. Field-swept echo-detected X-band EPR (left) and Davies ENDOR (right) spectra of **1**[BF_4] in butyronitrile at 15 K. Arrows indicate the positions where ENDOR spectra were detected. For details, see the Experimental Methods.

frequencies. No hyperfine splitting is expected (or observed) from the nickel center, because the isotopic distribution of nickel is such that ~99% of the nickel centers have no nuclear spin ($I = 0$). The **g** tensor anisotropy is not resolved at X-band, but mostly resolved at Q-band and completely resolved at D-band. Thus, the simulation of the Q-band and D-band spectra allowed the unequivocal determination of the electronic **g** tensor, which was used as a constraint for the simulation of the X-band spectrum; its principal values are 2.146(1), 2.063(1), and 2.017(1). The four ^{31}P hyperfine interaction tensors (**A** tensors) were obtained from simulation of X-band and Q-band spectra. These values are set out in Table 1. To limit the number of adjustable parameters for the fit of the spectra, the four ^{31}P **A** tensors were assumed to be identical and their principal axes to be collinear to the principal axes of the **g** tensor. As discussed below in the DFT section, the calculated ^{31}P coupling constants show very good agreement with those obtained by fit of the spectra.

The hyperfine coupling constants measured for $\mathbf{1}^+$ are clearly different from those reported previously for $\mathbf{4}^+$ [24] and $\mathbf{5}^+$ [25] (Table 1). The *g* values of $\mathbf{1}^+$ are different from those of $\mathbf{4}^+$. The *g* values of complex $\mathbf{5}^+$ are rather uncertain, since the authors did not resolve the **g** tensor in their EPR experiments, but obtained it by a multiparameter fit assuming isotropic ^{31}P hyperfine coupling. A clear comparison with the **g** tensor of $\mathbf{5}^+$ is thus not possible. Possible reasons for the marked sensitivity of the hyperfine couplings of these $[Ni(P^R_2N^{R'}_2)_2]^+$ complexes to the nature of the R/R′ substituents will be discussed below. The EPR spectra of **1**[BF_4] samples prepared in two different solvents, butyronitrile and 1:2 acetonitrile/dichloromethane, provided virtually identical magnetic resonance parameters (Table 1 and Supporting Information, Figure S5). These results, in combination with the hyperfine sublevel correlation spectroscopy (HYSCORE) experiment (described below), lead to the conclusion that the solvent molecules do not coordinate to the nickel ion in the Ni(I) oxidation state, and that the geometry of the $\mathbf{1}^+$ ion is essentially independent of the nature of these solvents. This is also supported by DFT calculations, which could not find a stable structure with acetonitrile ligating the Ni(I) ion while maintaining the four Ni−P bonds.

While the simulations of the X- and Q-band spectra nicely reproduce their ^{31}P hyperfine structure, the intensities are not perfectly fit in several parts of the spectrum (Figure 2). One possible reason is that the four ^{31}P hyperfine interaction tensors are not identical, from both principal values and principal axis systems with respect to the electronic **g** tensor axis system. This discrepancy could be caused by small distortions of the phosphorus nuclei from a symmetry-equivalent environment (idealized D_2 symmetry for the NiP_4 core). This possibility has also been noted in previous EPR studies of $\mathbf{4}^+$ and $\mathbf{5}^+$, for which the effects are more pronounced.[24,25] For $\mathbf{5}^+$ the simulation of the EPR spectrum yielded four different ^{31}P hyperfine coupling constants, and the gas-phase molecular structure calculated using DFT exhibited inequivalent Ni−P bond distances (d(Ni−P) = 2.22−2.23 Å).[25] It should be noted that, for $\mathbf{5}^+$, the multiparameter fit was restricted to isotropic ^{31}P hyperfine coupling. For $\mathbf{1}^+$, the crystal structure provides Ni−P bond distances that are equivalent and DFT calculations also provide a near idealized-symmetry structure. Small distortions of the compound under the conditions of the EPR experiment might result from geometric variations among the four six-membered $[NiP^{Cy}CH_2N^{tBu}CH_2P^{Cy}]$ rings present within $\mathbf{1}^+$, which then are trapped in the frozen solvent matrix. Consistent with this possibility, two conformations are observed for the free $P^{Cy}_2N^{tBu}_2$ ligand in solution at room temperature by NMR spectroscopy.[27] DFT calculations on $\mathbf{1}^+$ and $\mathbf{4}^+$ (see below) also point to marked differences between the symmetries and the energetic accessibility of other conformers for these ions.

To gain further insight into the hyperfine couplings with the ligand magnetic nuclei, which are a fingerprint of spin density distribution within the nearest surroundings, we performed pulsed ENDOR experiments at X-band. The contributions to these spectra from the strongly coupled ^{31}P nuclei are expected to lie in the 50−120 MHz frequency range. Accordingly, the ENDOR spectra exhibit several partially overlapping signals in the frequency region between 60 and 110 MHz. These signals show some dependence on the static magnetic field, confirming that all ^{31}P atoms have a considerable anisotropic contribution to the hyperfine interaction tensor (Supporting Information, Figures S6 and S7).

The low-frequency region of the ENDOR spectra is dominated by signals from ^{1}H nuclei coupled to the unpaired electron spin (Figure 3). The ^{1}H ENDOR spectra show weak orientation dependence, with the largest ^{1}H hyperfine coupling around 10 MHz. The larger of those couplings are attributed to ^{1}H nuclei near the nickel atom, which carries together with the phosphorus atoms the bulk of the spin density (see also the DFT section below). The nearest ^{1}H nuclei are those of the eight CH_2 groups connecting the phosphine and amine (at distances of 3.813−4.148 Å, on the basis of the crystal structure), and the four ^{1}H nuclei at the α position of the cyclohexyl groups (3.792 and 3.796 Å). The rest of the

DOI: 10.1021/acs.inorgchem.5b00445
Inorg. Chem. 2015, 54, 6226−6234

ENDOR lines (hyperfine coupling <6 MHz) are assigned to distant ^{1}H nuclei. Considering the large number of such protons, no reliable analysis is feasible. To determine how solvent ^{1}H nuclei contribute to the ENDOR spectra, Davies ENDOR measurements were also performed for samples in fully deuterated and fully protonated MeCN/CH_2Cl_2 (1:2) mixtures (Supporting Information, Figure S8). The comparison clearly shows that solvent ^{1}H nuclei contribute only to the matrix part of the ENDOR spectra, i.e., the spectral region close to the Larmor frequency. This means that they are only weakly dipolar coupled and distant from the paramagnetic center of $\mathbf{1}^{+}$.

No clear ENDOR signals attributable to ^{14}N are visible, which is not surprising due to the small hyperfine coupling and quadrupolar nature of this nucleus. To clarify the degree of hyperfine coupling with ^{14}N, we performed a HYSCORE[22,55] experiment at X-band. An advantage of the HYSCORE experiment compared to ENDOR spectroscopy is its high sensitivity to the nuclei in the (so-called) complete cancellation condition, i.e., when one of the ENDOR transition frequencies is negligibly small. This condition is often fulfilled at X-band for ^{14}N with small hyperfine coupling. The HYSCORE spectrum (Figure 4) exhibits typical ^{14}N quadrupole lines in the range of

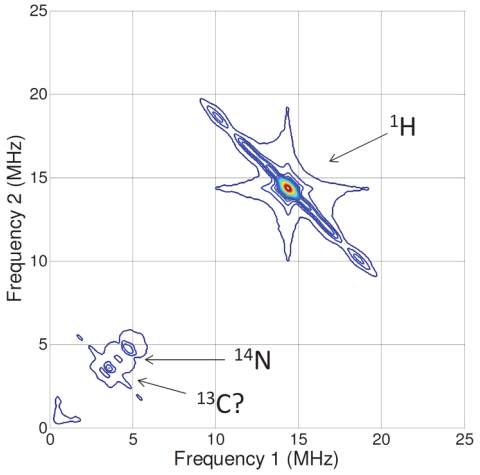

Figure 4. X-band HYSCORE spectra of $\mathbf{1}[BF_4]$ in butyronitrile at 20 K recorded at a magnetic field position of 336.5 mT. Arrows indicate the group of signals belonging to ^{14}N and ^{1}H nuclei. Signals centered at 3.6 MHz may partially stem from natural abundance ^{13}C (Supporting Information, Figure S9).

0−5 MHz. Simulation of the HYSCORE spectrum reveals that these lines are due to the relatively large quadrupole parameter, $e^2gQ/2h \approx 2.8$ MHz, and very small hyperfine coupling, $a_{iso} \approx$ 0.27 MHz (Supporting Information, Figure S9). DFT calculations on $\mathbf{1}^{+}$ confirm that there is negligible unpaired spin density on the nitrogen nuclei and that the ^{14}N hyperfine couplings are small ($A(^{14}N) < 1$ MHz; Supporting Information, Table S8). Out of diagonal signals centered around 3.6 MHz may be due to ^{13}C nuclei, which have a natural abundance of 1.1%. A corresponding simulation is shown in Figure S9. Signals in the 10−20 MHz range belong to ^{1}H resonances (the Larmor frequency of ^{1}H at 350 mT is ∼14.9 MHz). As for the ENDOR spectra, the HYSCORE spectrum reveals small anisotropy of ^{1}H hyperfine tensors with a maximum hyperfine coupling of about 10 MHz.

DFT Calculations on $[Ni(P^{R}_{2}N^{R'}_{2})_2]^{+}$ Complexes. The EPR spectra of $\mathbf{1}^{+}$ and hyperfine coupling constants derived therefrom are distinctly different from those reported previously for the related compounds $\mathbf{4}^{+}$[24] and $\mathbf{5}^{+}$.[25] In particular, the spectra for $\mathbf{1}^{+}$ are of higher resolution than those of the other compounds, despite the similar conditions employed in their measurement, and the ^{31}P hyperfine coupling constants are considerably smaller (Table 1). One possible reason for these differences is that the phosphine R and amine R′ substituents of $\mathbf{4}^{+}$ and $\mathbf{5}^{+}$ are similar to each other (R = Ph for $\mathbf{4}^{+}$ and $\mathbf{5}^{+}$; R′ = Ph for $\mathbf{4}^{+}$ or substituted phenyl for $\mathbf{5}^{+}$; Chart 1) but quite different, sterically and electronically, from those of $\mathbf{1}^{+}$ (R = Cy; R′ = *t*-Bu). To probe whether the nature of the ligand substituents could account for the differing experimental observations for these compounds, DFT calculations were performed of the structures and EPR parameters of $\mathbf{1}^{+}$ and $\mathbf{4}^{+}$. In addition, we computationally studied compounds $\mathbf{2}^{+}$ and $\mathbf{3}^{+}$, in which the R and R′ groups of $\mathbf{1}^{+}$ and $\mathbf{4}^{+}$ are permuted (Chart 1). Compounds $\mathbf{4}^{+}$ and $\mathbf{5}^{+}$ differ only in the nature of the *para* substituent on the amine phenyl group; thus, conclusions regarding the differences between $\mathbf{1}^{+}$ and $\mathbf{4}^{+}$ may also apply to differences between $\mathbf{1}^{+}$ and $\mathbf{5}^{+}$.

Selected metrical data for the calculated gas-phase structures of $\mathbf{1}^{+}$, $\mathbf{2}^{+}$, $\mathbf{3}^{+}$, and $\mathbf{4}^{+}$ are set out in Table 2; full details are reported in the Supporting Information, Tables S5−S25. The conclusion of primary importance from these data is that whereas $\mathbf{1}^{+}$, $\mathbf{2}^{+}$, and $\mathbf{3}^{+}$ are calculated to possess high-symmetry structures, the calculations for $\mathbf{4}^{+}$ provide three structures that are comparatively unsymmetrical. These structures represent discrete energy minima that lie within a few kilocalories per mole: $\mathbf{4a}^{+}$, relative energy 0 kcal/mol; $\mathbf{4b}^{+}$, relative energy +2.7 kcal/mol; $\mathbf{4c}^{+}$, relative energy +4.1 kcal/mol (energy differences and energetic ordering depending on the functional and basis set). In particular, for $\mathbf{1}^{+}$, $\mathbf{2}^{+}$, and $\mathbf{3}^{+}$, the four Ni−P bond lengths and two intraligand P−Ni−P bond angles are nearly identical for a given compound, yielding structures of

Table 2. Calculated (DFT) Bond Distances (Å) and Angles (deg) for $[Ni(P^{R}_{2}N^{R'}_{2})_2]^{+}$ Complexes $\mathbf{1}^{+}$, $\mathbf{2}^{+}$, $\mathbf{3}^{+}$, and $\mathbf{4}^{+}$ [a]

compd	R	R′	*d*(Ni−P)	∠(P−Ni−P)[b]	α[c]	β[d]
$\mathbf{1}^{+}$	Cy	*t*-Bu	2.225, 2.225, 2.225, 2.224	83.8	69.1	333.7
$\mathbf{2}^{+}$	Ph	*t*-Bu	2.245	83.1	71.6	334.3
$\mathbf{3}^{+}$	Cy	Ph	2.229	85.5	60.9	348.7
$\mathbf{4a}^{+}$ [e]	Ph	Ph	2.252, 2.243, 2.243, 2.248	85.0, 84.2	62.4	350.3
$\mathbf{4b}^{+}$ [e]	Ph	Ph	2.275, 2.246, 2.246, 2.275	84.9	56.7	354.8
$\mathbf{4c}^{+}$ [e]	Ph	Ph	2.267, 2.240, 2.235, 2.243	85.1, 86.3	59.2	355.0

[a]Only one distance or angle is listed when it applies to all linkages of that type within the compound. [b]Intraligand angle. [c]Dihedral angle between interligand P−Ni−P planes. [d]Average sum of three C−N−C angles each for four amine moieties. [e]These structures represent discrete energy minima: $\mathbf{4a}^{+}$, 0 kcal/mol; $\mathbf{4b}^{+}$, +2.7 kcal/mol; $\mathbf{4c}^{+}$, +4.1 kcal/mol. Energy differences and energetic ordering depending on the functional and basis set.

DOI: 10.1021/acs.inorgchem.5b00445
Inorg. Chem. 2015, 54, 6226−6234

Table 3. Calculated (DFT) and Experimental EPR Parameters for $[Ni(P^R_2N^{R'}_2)_2]^+$ Complexes[a]

	g value		^{31}P hyperfine coupling constant (MHz)	
compd	calcd	exptl	calcd	exptl
1^+	2.1612, 2.0635, 2.0454	2.146, 2.063, 2.017	154, 160, 203	150, 160, 185
2^+	2.1899, 2.0806, 2.0611	na	142, 148, 185	na
3^+	2.1385, 2.0519, 2.0398	na	170, 178, 224	na
4^+		2.104, 2.070, 2.006		210, 220, 220
$4a^+$ [b]	2.1607, 2.0651, 2.0469	na	173, 180, 221	na
			166, 172, 215	
			161, 168, 209	
			159, 166, 206	
$4b^+$ [c]	2.1478, 2.0600, 2.0490	na	199, 204, 238	na
			178, 183, 229	
$4c^+$ [b]	2.1443, 2.0596, 2.0470	na	177, 184, 226	na
			192, 198, 242	
			190, 196, 235	
			172, 176, 211	

[a] **A** tensors with hyperfine coupling constants within 1 MHz are assumed to be identical. [b] Four structurally inequivalent phosphorus nuclei; see Table 2. [c] Two pairs of structurally inequivalent phosphorus nuclei; see Table 2.

approximate D_2 symmetry. For 4^+, in contrast, each of the three calculated structures has several different Ni−P bond lengths and P−Ni−P bond angles. The previously reported calculated structure for 5^+, which is compositionally similar to 4^+, was also noted to have inequivalent Ni−P bond lengths (2.22−2.23 Å).[25] These findings are consistent with the observations, noted in the previous section, that the EPR spectroscopic simulations for 1^+ evince a high-symmetry molecular structure about the nickel center, while those for 4^+ are consistent with a lower symmetry structure. The EPR spectra of 5^+ are qualitatively similar to those of 4^+, consistent with it possessing similar structure-controlling R and R′ groups.

Pairwise comparisons among the metrical data for these compounds allow the structural consequences of their R and R′ groups to be elucidated. Compounds 1^+ and 3^+ possess the same phosphine R group (Cy) but differ in their second-coordination-sphere amine R′ groups (1^+, *t*-Bu; 3^+, Ph). The change in the remote substituent has consequences both for the structure about the amine and for the NiP_4 core. Compared to 1^+, the geometries of the amine moieties of 3^+ are closer to planar, with the sum of their C−N−C angles (β) being larger by 15° (3^+, 348.7°; 1^+, 333.7°) and the angle within the CH_2−N−CH_2 tether increasing from 111.2° (1^+) to 114.8° (3^+). These structural differences affect the geometry about the nickel center, as evidenced by the fact that 3^+ exhibits a larger P−Ni−P bite angle (85.5°) than that calculated for 1^+ (83.8°) and, strikingly, by the interligand dihedral angle (α), which is notably smaller for 3^+ (60.9°) than for 1^+ (69.1°) despite their identical phosphine R groups. The Ni−P bond lengths are not significantly impacted by the change in R′. A similar comparison of the calculated structures for 1^+ and 2^+ reveals the consequences of changing the phosphine R substituent from Cy to Ph while keeping the amine R′ substituent constant (*t*-Bu). Unsurprisingly, this first-coordination-sphere substitution affects the calculated Ni−P bond lengths, with those for 2^+ (2.245 Å) being slightly longer than those for 1^+ (2.225 Å). However, by most other metrics, the overall molecular structure is *less* perturbed by this substitution in R than by the R′ variation between 1^+ and 3^+. Specifically, 1^+ and 2^+ exhibit more closely similar P−Ni−P bite angles (83.8° and 83.1°, respectively), interligand dihedral angles α (69.1° and 71.6°), and amine bond angle sums β (333.7° and 334.3°) than do 1^+ and 3^+. These group-specific structural perturbations carry over to 4^+, which possesses the same phosphine R group as 2^+ and amine R′ group as 3^+. Compared to 1^+, $4a^+$ exhibits the longer R-controlled Ni−P distances found for 2^+, and variations in the R′-controlled P−Ni−P, α, and β angles that are similar to those for 3^+. However, the combination in 4^+ of these R and R′ structural perturbations results in conformational strains within the $P^R_2N^{R'}_2$ ligands that cannot be accommodated by a high-symmetry structure of the types observed for 1^+, 2^+, and 3^+, as manifested by the observation of marked inequivalences among its chemically related bond distances and angles and three computed close-lying structural local minima.

In addition to the different molecular symmetries found for 1^+ and 4^+, the calculated magnetic parameters of these ions also differ significantly from each other. These results are set out in Table 3, in which phosphorus (^{31}P) hyperfine couplings are given as principal values A_x, A_y, and A_z to allow a better comparison to the experimental values. The orientations of the principal axis systems are provided in the Supporting Information (Figure S10, Tables S8−S25). For 1^+, the calculated *g* values and ^{31}P hyperfine coupling constants are seen to be in good agreement with those observed experimentally. Inasmuch as the experimental magnetic parameters of 1^+ are derived from well-resolved EPR spectra, this level of agreement suggests that the computational methodology is adequate to predict trends in magnetic parameters as a function of the ligand substituent and geometry.

The phosphorus hyperfine coupling constants of 1^+ are considerably smaller than those for 4^+. Because the three calculated structures of 4^+ are of lower symmetry, multiple hyperfine coupling constants are provided for each chemically distinct phosphorus nucleus. Although this prevents direct comparison to the experimental values, simple averaging indicates that the calculated values for 4^+ are larger than those calculated for 1^+, in line with experimental observations for the two compounds. It is also striking how different the hyperfine coupling constants are for a given conformer of 4^+, and how significantly different the values of 1^+ and 4^+ are from those of their R/R′-permuted analogues 2^+ and 3^+. This highlights both the high sensitivity of these values to structural

DOI: 10.1021/acs.inorgchem.5b00445
Inorg. Chem. 2015, 54, 6226−6234

perturbations and the challenges associated with elucidating them from experiment, especially in frozen solutions in which multiple conformers may be found even for "symmetric" compounds.

The smaller ^{31}P hyperfine coupling constants of $\mathbf{1}^+$ relative to $\mathbf{4}^+$ and $\mathbf{5}^+$ indicate that there are differences in the delocalization onto the ligands of the unpaired spin. The calculated spin densities for $\mathbf{1}^+$ and $\mathbf{4b}^+$ are shown in Figure 5.

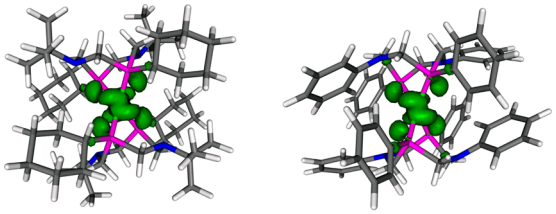

Figure 5. Calculated electron spin densities for complexes $\mathbf{1}^+$ and $\mathbf{4b}^+$ at the 0.002 e/a_0^3 isosurface level. Note that spin density distributions for all $\mathbf{4}^+$ structures look identical. Additional views at smaller isosurface levels are shown in the Supporting Information (Figures S11 and S12).

It is apparent that, for both, the primary location of electron spin density is on the nickel atom and the four attached phosphorus atoms. Complex $\mathbf{1}^+$ has 75.8% of the Mulliken spin density located on nickel, with the four phosphorus atoms having nearly equivalent percentages of 4.6% each for a total of 18.4%. The remaining amount is distributed over the ligand with no single atom having greater than 0.7%. For $\mathbf{4}^+$, the Mulliken spin density is on average 74.4% ($\mathbf{4a}^+$, 76.2%; $\mathbf{4b}^+$, 73.9%; $\mathbf{4c}^+$, 73.2%) on nickel and 19.7% ($\mathbf{4a}^+$, 19.6%; $\mathbf{4b}^+$, 19.8%; $\mathbf{4c}^+$, 19.7%) on phosphorus. The relative change in spin density distribution between $\mathbf{1}^+$ and $\mathbf{4}^+$ is more pronounced on the phosphorus than on the nickel atom. Qualitatively, the increased spin density on the phosphorus atoms for $\mathbf{4}^+$ as compared to $\mathbf{1}^+$ is consistent with the larger hyperfine coupling constants for the former. The increased phosphorus spin density is also qualitatively consistent with the fact that the phosphine R group of $\mathbf{4}^+$ (Ph) is electron-withdrawing relative to that of $\mathbf{1}^+$ (Cy), as manifested broadly among metal–phosphine compounds through the stronger π back-bonding to arylphosphines than to alkylphosphines.[58] In the present case, however, the precise contribution of the electron-withdrawing nature of the R group to the phosphorus spin densities is difficult to disentangle from geometric factors, which include the pronounced differences in R′-controlled bond and dihedral angles between $\mathbf{1}^+$ and $\mathbf{4}^+$.

SUMMARY AND CONCLUSIONS

Crystallographic, DFT computational, and multifrequency EPR spectroscopic studies of the hydrogen oxidation catalyst $[Ni(P^{Cy}_2N^{tBu}_2)_2]^+$ ($\mathbf{1}^+$) have provided a number of insights into its intrinsic properties and how these differ from those of previously studied proton reduction catalysts of the broader $[Ni(P^R_2N^{R'}_2)_2]^{n+}$ family. The EPR and ENDOR spectra allowed determination of the electronic **g** tensor and the ^{31}P hyperfine coupling constants, and together with HYSCORE experiments demonstrated that the hyperfine couplings of the ^{1}H and ^{14}N nuclei to the unpaired spin are intermediate and weak, respectively. The EPR spectroscopic data do not exhibit evidence of coordination to the Ni(I) center by the potentially ligating solvents acetonitrile and butyronitrile. The EPR spectra observed for $\mathbf{1}^+$ are of higher resolution and evince a higher symmetry molecular geometry than those reported previously for $Ni(P^{Ph}_2N^{Ph}_2)_2]^+$ ($\mathbf{4}^+$) and $Ni(P^{Ph}_2N^{Ar'}_2)_2]^+$ ($\mathbf{5}^+$). Consistent with this, crystallographic and DFT computational studies of $\mathbf{1}^+$ demonstrate that the NiP_4 core structure is highly symmetric in the solid state and gas phase, respectively. In contrast, the proton reduction catalyst $[Ni(P^{Ph}_2N^{Ph}_2)_2]^+$ ($\mathbf{4}^+$) is calculated to possess (at least) three less symmetrical conformers that are separated in energy by only a few kilocalories per mole. The distorted structure found for $\mathbf{4}^+$ results from a combination of specific R- and R′-controlled geometric perturbations, as deduced from the calculated structures of the R/R′-permuted analogues $[Ni(P^{Ph}_2N^{tBu}_2)_2]^+$ ($\mathbf{2}^+$) and $[Ni(P^{Cy}_2N^{Ph}_2)_2]^+$ ($\mathbf{3}^+$). It is especially noteworthy that, with the exception of the Ni–P bond length, the structural consequences of the remote R′ amine substituent exceed those of the first-coordination-sphere phosphine R substituent, and that both substituents are calculated to have profound effects on the ^{31}P hyperfine coupling constant. The larger ^{31}P hyperfine coupling constants observed for $\mathbf{4}^+$ relative to $\mathbf{1}^+$ reflect greater spin density delocalization onto the ligands, as supported by DFT calculations.

These results raise the question of whether the molecular and electronic structures of $[Ni(P^R_2N^{R'}_2)_2]^+$ complexes are generally as strongly dependent on the nature of the remote amine R′ group as they are upon the first-coordination-sphere R phosphine group, as found here for $\mathbf{1}^+$ and $\mathbf{4}^+$. The combined experimental approaches described in this Article appear suitable to shed light on both this question and the extent to which these effects influence the catalytic activity of this important class of catalysts.

ASSOCIATED CONTENT

Supporting Information

X-ray crystallographic data in CIF format, X-ray crystal structure details of $\mathbf{1}[BF_4]$, additional EPR/ENDOR spectra, HYSCORE simulations, and details of the DFT calculations. The Supporting Information is available free of charge on the ACS Publications website at DOI: 10.1021/acs.inorgchem.5b00445.

AUTHOR INFORMATION

Corresponding Authors

*E-mail: mhopkins@uchicago.edu.
*E-mail: oleg@anl.gov.

Notes

The authors declare no competing financial interest.

ACKNOWLEDGMENTS

This material is based upon work supported by the U.S. Department of Energy, Office of Science, Office of Basic Energy Sciences, Division of Chemical Sciences, Geosciences, and Biosciences, under Contract Numbers DE-AC02-06CH11357 at Argonne National Laboratory (J.N. and O.G.P.) and DE-FG02-07-ER15910 (M.W. and M.D.H.). K.L.M. was supported by the Illinois Space Grant Consortium, and T.L.B. and A.M.P.-M. were supported by a National Institutes of Health National Institute of General Medical Sciences (NIGMS) Grant (R25 GM59218). We thank Dr. Ian Steele and Dr. Alex Filatov for determining the crystal structure.

DOI: 10.1021/acs.inorgchem.5b00445
Inorg. Chem. 2015, 54, 6226–6234

REFERENCES

(1) Cook, T. R.; Dogutan, D. K.; Reece, S. Y.; Surendranath, Y.; Teets, T. S.; Nocera, D. G. *Chem. Rev.* **2010**, *110*, 6474−6502.
(2) Lewis, N. S.; Nocera, D. G. *Proc. Natl. Acad. Sci. U.S.A.* **2006**, *103*, 15729−15735.
(3) Balzani, V.; Credi, A.; Venturi, M. *ChemSusChem* **2008**, *1*, 26−58.
(4) Simmons, T. R.; Artero, V. *Angew. Chem., Int. Ed.* **2013**, *52*, 6143−6145.
(5) Eckenhoff, W. T.; McNamara, W. R.; Du, P. W.; Eisenberg, R. *Biochim. Biophys. Acta, Bioenerg.* **2013**, *1827*, 958−973.
(6) Eckenhoff, W. T.; Eisenberg, R. *Dalton Trans.* **2012**, *41*, 13004−13021.
(7) Carroll, M. E.; Barton, B. E.; Rauchfuss, T. B.; Carroll, P. J. *J. Am. Chem. Soc.* **2012**, *134*, 18843−18852.
(8) DuBois, D. L. *Inorg. Chem.* **2014**, *53*, 3935−3960.
(9) Gloaguen, F.; Rauchfuss, T. B. *Chem. Soc. Rev.* **2009**, *38*, 100−108.
(10) McKone, J. R.; Marinescu, S. C.; Brunschwig, B. S.; Winkler, J. R.; Gray, H. B. *Chem. Sci.* **2014**, *5*, 865−878.
(11) Shaw, W. J.; Helm, M. L.; DuBois, D. L. *Biochim. Biophys. Acta, Bioenerg.* **2013**, *1827*, 1123−1139.
(12) Bullock, R. M.; Appel, A. M.; Helm, M. L. *Chem. Commun.* **2014**, *50*, 3125−3143.
(13) DuBois, D. L.; Bullock, R. M. *Eur. J. Inorg. Chem.* **2011**, 1017−1027.
(14) DuBois, M. R.; DuBois, D. L. *Acc. Chem. Res.* **2009**, *42*, 1974−1982.
(15) O'Hagan, M.; Ho, M. H.; Yang, J. Y.; Appel, A. M.; DuBois, M. R.; Raugei, S.; Shaw, W. J.; DuBois, D. L.; Bullock, R. M. *J. Am. Chem. Soc.* **2012**, *134*, 19409−19424.
(16) O'Hagan, M.; Shaw, W. J.; Raugei, S.; Chen, S. T.; Yang, J. Y.; Kilgore, U. J.; DuBois, D. L.; Bullock, R. M. *J. Am. Chem. Soc.* **2011**, *133*, 14301−14312.
(17) Raugei, S.; Chen, S. T.; Ho, M. H.; Ginovska-Pangovska, B.; Rousseau, R. J.; Dupuis, M.; DuBois, D. L.; Bullock, R. M. *Chem.−Eur. J.* **2012**, *18*, 6493−6506.
(18) Yang, J. Y.; Smith, S. E.; Liu, T.; Dougherty, W. G.; Hoffert, W. A.; Kassel, W. S.; DuBois, M. R.; DuBois, D. L.; Bullock, R. M. *J. Am. Chem. Soc.* **2013**, *135*, 9700−9712.
(19) Chen, S. T.; Ho, M. H.; Bullock, R. M.; DuBois, D. L.; Dupuis, M.; Rousseau, R.; Raugei, S. *ACS Catal.* **2014**, *4*, 229−242.
(20) Bencini, A.; Gatteschi, D. *EPR of Exchange Coupled Systems*; Springer-Verlag: Berlin, 1990.
(21) Abragam, A.; Bleaney, B. *Electron Paramagnetic Resonance of Transition Ions*; Dover: New York, 1986.
(22) Schweiger, A.; Jeschke, G. *Principles of Pulse Electron Paramagnetic Resonance*; Oxford University Press: New York, 2001.
(23) Pilbrow, J. R. *Transition Ion Electron Paramagnetic Resonance*; Clarendon Press: New York, 1991.
(24) Silver, S. C.; Niklas, J.; Du, P. W.; Poluektov, O. G.; Tiede, D. M.; Utschig, L. M. *J. Am. Chem. Soc.* **2013**, *135*, 13246−13249.
(25) Kochem, A.; Neese, F.; van Gastel, M. *J. Phys. Chem. C* **2014**, *118*, 2350−2360.
(26) Kochem, A.; Weyhermüller, T.; Neese, F.; van Gastel, M. *Organometallics* **2015**, *34*, 995−1000.
(27) Yang, J. Y.; Chen, S. T.; Dougherty, W. G.; Kassel, W. S.; Bullock, R. M.; DuBois, D. L.; Raugei, S.; Rousseau, R.; Dupuis, M.; DuBois, M. R. *Chem. Commun.* **2010**, *46*, 8618−8620.
(28) Stolley, R. M.; Darmon, J. M.; Helm, M. L. *Chem. Commun.* **2014**, *50*, 3681−3684.
(29) Pangborn, A. B.; Giardello, M. A.; Grubbs, R. H.; Rosen, R. K.; Timmers, F. J. *Organometallics* **1996**, *15*, 1518−1520.
(30) Fulmer, G. R.; Miller, A. J. M.; Sherden, N. H.; Gottlieb, H. E.; Nudelman, A.; Stoltz, B. M.; Bercaw, J. E.; Goldberg, K. I. *Organometallics* **2010**, *29*, 2176−2179.
(31) Davies, E. R. *Phys. Lett. A* **1974**, *47*, 1−2.
(32) Gemperle, C.; Schweiger, A. *Chem. Rev.* **1991**, *91*, 1481−1505.
(33) Mims, W. B. *Proc. R. Soc. London, A* **1965**, *283*, 452−457.
(34) Hyde, J. S.; Pasenkiewicz-Gierula, M.; Jesmanowicz, A.; Antholine, W. E. *Appl. Magn. Reson.* **1990**, *1*, 483−496.
(35) Poluektov, O. G.; Utschig, L. M.; Schlesselman, S. L.; Lakshmi, K. V.; Brudvig, G. W.; Kothe, G.; Thurnauer, M. C. *J. Phys. Chem. B* **2002**, *106*, 8911−8916.
(36) Bresgunov, A. Y.; Dubinskii, A. A.; Krimov, V. N.; Petrov, Y. G.; Poluektov, O. G.; Lebedev, Y. S. *Appl. Magn. Reson.* **1991**, *2*, 715−728.
(37) Epel, B.; Gromov, I.; Stoll, S.; Schweiger, A.; Goldfarb, D. *Concepts Magn. Reson., B* **2005**, *26*, 36−45.
(38) Niklas, J.; Mardis, K. L.; Rakhimov, R. R.; Mulfort, K. L.; Tiede, D. M.; Poluektov, O. G. *J. Phys. Chem. B* **2012**, *116*, 2943−2957.
(39) Stoll, S.; Schweiger, A. *J. Magn. Reson.* **2006**, *178*, 42−55.
(40) Baker, J.; Wolinski, K.; Malagoli, M.; Kinghorn, D.; Wolinski, P.; Magyarfalvi, G.; Saebo, S.; Janowski, T.; Pulay, P. *J. Comput. Chem.* **2009**, *30*, 317−335.
(41) Neese, F. *WIREs Comput. Mol. Sci.* **2012**, *2*, 73−78.
(42) Neese, F. *J. Chem. Phys.* **2001**, *115*, 11080−11096.
(43) Stephens, P. J.; Devlin, F. J.; Chabalowski, C. F.; Frisch, M. J. *J. Phys. Chem.* **1994**, *98*, 11623−11627.
(44) Becke, A. D. *J. Chem. Phys.* **1993**, *98*, 5648−5652.
(45) Lee, C. T.; Yang, W. T.; Parr, R. G. *Phys. Rev. B: Condens. Matter* **1988**, *37*, 785−789.
(46) Vosko, S. H.; Wilk, L.; Nusair, M. *Can. J. Phys.* **1980**, *58*, 1200−1211.
(47) Rega, N.; Cossi, M.; Barone, V. *J. Chem. Phys.* **1996**, *105*, 11060−11067.
(48) Barone, V. In *Recent Advances in Density Functional Methods*; Chong, D. P., Ed.; World Scientific: Singapore, 1995; Part 1, pp 287−334.
(49) Kutzelnigg, W.; Fleischer, U.; Schindler, M. In *Deuterium and Shift Calculation*; Diehl, P., Fluck, E., Günther, H., Kosfeld, R., Seelig, J., Eds.; Springer-Verlag: Berlin, 1990; Vol. 23.
(50) Wachters, A. J. H. *J. Chem. Phys.* **1970**, *52*, 1033−1036.
(51) Wachters, A. J. H. *IBM Technical Report RJ. 584*; IBM: San Jose, CA, 1969.
(52) Bauschlicher, C. W.; Langhoff, S. R.; Partridge, H.; Barnes, L. A. *J. Chem. Phys.* **1989**, *91*, 2399−2411.
(53) Weigend, F.; Ahlrichs, R. *Phys. Chem. Chem. Phys.* **2005**, *7*, 3297−3305.
(54) Wiedner, E. S.; Yang, J. Y.; Chen, S. T.; Raugei, S.; Dougherty, W. G.; Kassel, W. S.; Helm, M. L.; Bullock, R. M.; DuBois, M. R.; DuBois, D. L. *Organometallics* **2012**, *31*, 144−156.
(55) Höfer, P.; Grupp, A.; Nebenfuhr, H.; Mehring, M. *Chem. Phys. Lett.* **1986**, *132*, 279−282.
(56) Hartwig, J. F. *Organotransition Metal Chemistry*; University Science Books: Mill Valley, CA, 2010; pp 36−37.

DOI: 10.1021/acs.inorgchem.5b00445
Inorg. Chem. 2015, 54, 6226−6234